

we conclude that the sample is chemically inhomogeneous, that the  $\text{Li}^+$  comes from the same source as  $\text{Na}^+$ , and that the mass-91 ions come from a different source than either  $\text{Na}^+$  or  $\text{Li}^+$ . This same argument holds for several other species as well. The peaks associated with PS generally have <1% coincidence with  $\text{Na}^+$  whereas those associated with NaF have >5% coincidence with  $\text{Na}^+$  (Fig. 4).

For a more precise comparison between the two groups, one can also attempt to fit the experimental data to the model. Given that the sample is composed of  $\sim 0.5\text{-}\mu\text{m}$  NaF crystals on PS and that the coverage of these crystals on the PS surface is  $\sim 3\%$ , one finds that  $P_{\text{homo}}(\text{M}^+, \text{Na}^+)$ , where  $\text{M}^+$  is an arbitrary mass ion, is a factor of  $\sim 70$  greater than  $P_{\text{in}}(\text{M}^+, \text{Na}^+)$ . In Fig. 4,  $P_{\text{in}}(\text{M}^+, \text{Na}^+)$  is represented by the group of points associated with PS, whereas  $P_{\text{homo}}(\text{M}^+, \text{Na}^+)$  is represented by the group of points associated with NaF. From the plot, one observes that  $\%_{\text{homo}}(\text{M}^+, \text{Na}^+)$  is only a factor of 15 greater than  $\%_{\text{in}}(\text{M}^+, \text{Na}^+)$ . This factor is lower than that predicted by the model because the NaF crystals are not squares as the model assumes. As noted earlier, irregularly shaped NaF crystals lead to a longer interface between the NaF and the PS and larger values for  $\%_{\text{in}}(\text{M}^+, \text{Na}^+)$  than are expected by the model. Nevertheless, the difference in the percent coincidences of more than an order of magnitude between the two groups supports the conclusion that the polystyrene is indeed spatially well separated from the NaF.

This example demonstrates the use of coincidence counting with TOF mass spectroscopy in the analysis of surfaces for chemical homogeneity at the 100-nm level. In principle, the technique should have an ultimate resolution of about 10 nm, that is, the diameter of the sample spot addressed by an individual primary ion (9). In practice, the resolution limit is set by the length of the interface of highly irregularly shaped inhomogeneities in the sample. The coincidence spectra may also be useful in revealing chemical relations between secondary ions and in the separation of mass spectrometric signal from background. Further, coincidence counting may be useful in examining the kinetic energy relations of secondary ions and the relation of secondary ions to secondary electrons.

#### REFERENCES AND NOTES

1. L. Schmidt and H. Jungclas, *Lect. Notes Phys.* **269**, 234 (1986).
2. A. Hedin, P. Hakansson, B. U. R. Sundqvist, *Int. J. Mass Spectrom. Ion Processes* **77**, 123 (1987).
3. N. Furstenua, *Z. Naturforsch.* **33a**, 563 (1978).
4. ———, W. Knippelberg, F. R. Krueger, G. Weiss, K. Wien, *ibid.* **32a**, 711 (1977).
5. R. D. Macfarlane, *Anal. Chem.* **55**, 1247A (1983).
6. L. Q. Huang, R. J. Conzemius, G. A. Junk, R. S. Houk, *Int. J. Mass Spectrom. Ion Processes* **90**, 85 (1989).
7. S. Della Negra, D. Jacquet, I. Lorthiois, Y. Le Beyec, *Int. J. Mass Spectrom. Ion Phys.* **53**, 215 (1983).
8. W. R. Summers and E. A. Schweikert, *Rev. Sci. Instrum.* **57**, 692 (1986).
9. K. Wien, *Lect. Notes Phys.* **269**, 1 (1986).
10. G. Bolbach *et al.*, *Nucl. Instrum. Methods Phys. Res.* **B30**, 74 (1988).
11. E. Festa and R. Sellem, *Nucl. Instrum. Methods* **188**, 99 (1981).
12. We thank C. H. Spiegelman of the Department of Statistics at Texas A&M University for consultation on the statistical models described above.

12 December 1989; accepted 4 April 1990

## Image Reconstruction of the Interior of Bodies That Diffuse Radiation

J. R. SINGER, F. ALBERTO GRÜNBAUM, PHILIP KOHN,  
JORGE PASSAMANI ZUBELLI

A method for reconstructing images from projections is described. The unique aspect of the procedure is that the reconstruction of the internal structure can be carried out for objects that diffuse the incident radiation. The method may be used with photons, phonons, neutrons, and many other kinds of radiation. The procedure has applications to medical imaging, industrial imaging, and geophysical imaging.

**I**N THIS REPORT WE DESCRIBE A PROCEDURE to determine and display images of the internal structure of objects that diffuse radiation. Such objects are members of a large class. For example, the human body diffuses infrared radiation, ultrasonic radiation, and neutrons. Almost all solids are also in this class. It is difficult to specify a substance in which diffusion along with absorption does not occur for some form of radiation.

We began studying the transmission of infrared laser beams through animal tissues. The projections of diffusely transmitted radiation could be observed by silicon detector arrays and displayed on a video screen. For tissues up to about 2 cm thick, we could observe shadowgraphs of internal structures. Thicker tissues produced fuzzier shadowgraphs until the internal structures became difficult to delineate. Conventional techniques for reconstructing multiple projections by Cormack (1), Hounsfield (2), Boyd (3), and others for application to computer tomography were not helpful in reconstructing our diffused projections. We did observe that considerable information about internal structures existed within these projections. This observation prompted our research into methods of reconstructing internal images of objects utilizing a large collection of shadowgraphs.

The problem was to develop a method of image reconstruction that could utilize the diffused image projections and reconstruct

internal features of the diffusing object. The simplest case is a homogeneous slab with no internal structure with a particle beam directed at the face of the slab. This ideal example has been completely solved by Feynman and Hibbs (4). However, imaging the interior of a homogeneous body provides minimal information because there is no interior structure. In imaging more complex objects, we use the Feynman concept of summing the emergent particles over all possible paths (5). The resultant pattern of emergent particles will therefore contain the "history" of these paths.

To reconstruct the interior structure of an object containing inhomogeneities, we make the following assumptions:

1) Divide the object into volume elements (voxels); set the size of the voxels to be the desired resolution. (When dealing with the two-dimensional case, each element is termed a pixel.)

2) The particle beam enters the object at a series of points sequentially in time.

3) The particles of the beam may enter and leave each voxel, if not annihilated by absorption within the voxel. The absorption probability is  $\nu_{ijk}$  per voxel, and the survival probability is  $w_{ijk}$  per voxel, where  $w_{ijk} = 1 - \nu_{ijk}$ . The scattered probabilities for each voxel are  $f_{ijk}$  = forward scatter probability,  $b_{ijk}$  = backward scatter probability,  $s_{ijk}$  = sideways scatter probability, and we assume that  $b_{ijk} = 1 - 4s_{ijk} - f_{ijk}$ . The probability of a forward scatter is given by  $w_{ijk} \cdot f_{ijk}$ ; the probability of a backward scatter is  $w_{ijk} \cdot b_{ijk}$ ; the probability of a sideways scatter is  $w_{ijk} \cdot s_{ijk}$ .

4) For each voxel we provide the variables  $w$ ,  $f$ ,  $b$ , and  $s$ . As pointed out above, these reduce to three variables.

J. R. Singer, Electrical Engineering and Computer Science, and Biophysics Departments, University of California, Berkeley, CA 94720.  
F. A. Grünbaum and J. P. Zubelli, Mathematics Department, University of California, Berkeley, CA 94720.  
P. Kohn, International Computer Sciences Institute, University of California, Berkeley, CA 94720.

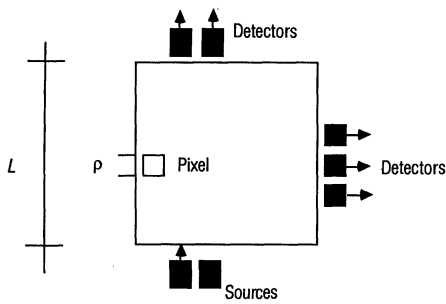


Fig. 1. Pictorial description of a source and a detector array in an arbitrary position.

5) We provide a detector array to detect the particles emergent from the object. The relative quantities of the emergent particles (the intensities) are inputs to a computer system.

6) Within a voxel, particles are either absorbed or are scattered to their nearest neighbors.

The imaging procedure uses a beam of particles directed at the surface of the object; the beam is sequentially directed at all available peripheral surfaces. The diffuse radiation emerging from the object is collected by an array of particle detectors that detect relative intensities, as schematically shown in Fig. 1. The intensity values are converted to digital form by an analog-to-digital converter and then stored in a computer memory system. A set of output values are obtained for each beam position. If the entire object is scanned by the input beam and the diffuse radiation is collected for all of the available positions, then a complete set of data is obtained.

A complete set provides much more data than is needed for the reconstruction; generally a partial set is utilized. A partial set is more practicable in imaging because some of the surfaces of the object may not be accessible, or because some of the surfaces may not be accessible to both the beam source and the detector array.

Each particle path is convoluted because of multiple scattering. In general, the problem of reconstruction is three dimensional. For ease of explanation, however, we will discuss a two-dimensional system. Generalization to the three-dimensional case is straightforward, and is described within the discussion.

The term "forward solution" refers to the following scenario: if we know the values of  $w_{ij}$ ,  $f_{ij}$ ,  $b_{ij}$ , and  $s_{ij}$  for all the voxels in the object, and we beam a known amount of radiation at a specified voxel on the periphery of the object, we can compute the amount of radiation that will be detected by each of the detectors around the object. In other words, the forward solution is the process of computing the values of the

external variables, that is, the detected radiation values. This is accomplished by setting up a system of linear equations for the probabilities  $P_{lk}$  that a particle inserted at beam position  $k$  will emerge at detector position  $l$ .

The "inverse solution" is a method of solving the following problem: given a set of intensity measurements obtained by using an array of detectors, compute the  $w_{ij}$ ,  $f_{ij}$ ,  $b_{ij}$ , and  $s_{ij}$  coefficients for all the pixels in the object being imaged. In other words, the inverse solution is the solution to the primary problem of reconstruction of the interior of the object, with the relative detected radiation intensities,  $P_{lk}$ , as the only known parameters.

Generally speaking, the inverse solution is an iterative process that works as follows. One first takes the required measurements and then makes an initial guess as to the values of the  $w_{ij}$ ,  $f_{ij}$ ,  $b_{ij}$ , and  $s_{ij}$  coefficients for all the voxels in the object. If the initial guess is based on the expected structure inside the object, that may substantially improve the speed with which the inverse solution is computed. However, for the purposes of testing the first prototypes, we have used an initial set of values corresponding to an object of uniform qualities, such as  $w_{ij} = 0.5$ ,  $f_{ij} = 0.7$ ,  $b_{ij} = 0.1$ , and  $s_{ij} = 0.1$  for all voxels inside the object.

Next, given the current values of the attenuation and scattering coefficients, the imaging system computes the expected intensities at each of the detectors' positions. In other words, one uses the above-described "forward solution" to compute how much radiation would emerge from the object at each detector position if the object's interior were accurately modeled by the currently assumed values of the attenuation and scattering coefficients.

Then, one determines the differences between the computed detector intensity values and those measured. More specifically, if we let  $P_{lk}$  be the measured intensity at sensor  $l$  with the source at position  $k$ , and  $c_{lk}$  the corresponding computed intensity, then our problem consists in minimizing:

$$E = \sum_{l=1}^{N_d} \sum_{k=1}^{N_s} (P_{lk} - c_{lk})^2 \quad (1)$$

where  $N_d$  and  $N_s$  are the total number of detectors and sources, respectively (Fig. 1).

Using special minimization techniques we adjust the values of the coefficients  $w_{ijk}$ ,  $f_{ijk}$ , and  $s_{ijk}$  (or  $w_{ij}$ ,  $f_{ij}$ , and  $s_{ij}$  in the two-dimensional case) until the error  $E$  is below a chosen threshold. This brings in some of the mathematical difficulties of this problem, namely, how to avoid local minima, as discussed in the next section. The general class of minimization methods used here are

called "gradient descent methods." See, for example, Press *et al.* (6). In summary, the gradient descent method produces an updated set of coefficients that will better match the actual radiation propagation characteristics of the object being imaged.

Once the iterative computation process is completed, a series of images is generated from the computed coefficient values. For instance, the system will typically draw an image in which the darkness or color of each point corresponds to the attenuation coefficient  $w_{ij}$  of the corresponding pixel; and another image in which the darkness or color of each point corresponds to the side-ways scattering coefficient  $s_{ij}$ . Images based on the backwards and forward scattering coefficients  $b_{ij}$  and  $f_{ij}$  are also generated to depict different characteristics of the object.

Referring to Fig. 2, A and B, there is shown in Fig. 2A a map of the attenuation characteristics of a two-dimensional simulated object. Using the procedures described here, we reconstructed the attenuation characteristics of this object, resulting in the map shown in Fig. 2B. More specifically, Fig. 2B is a map of the computed  $v_{ij}$  coefficients (equal to  $1 - w_{ij}$ ) for the object.

It is interesting to note that while the reconstructed image in Fig. 2B is generally quite accurate, the one portion of the object

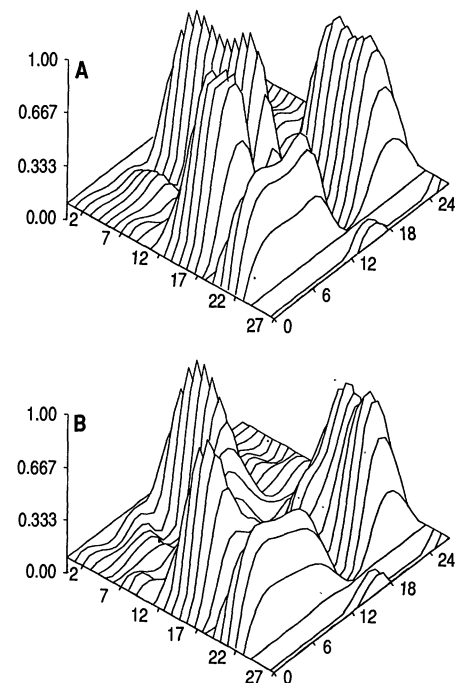
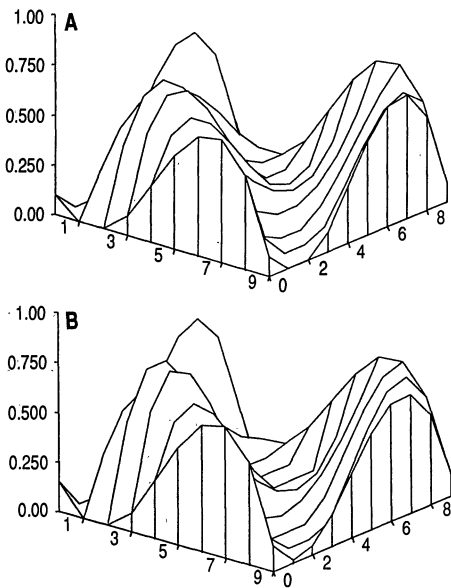


Fig. 2. (A) A simulated two-dimensional diffusing object (a phantom) which has attenuation values plotted as the hills (heights). The  $x$  and  $y$  coordinates are those of the object. (B) The reconstruction of the phantom object using the diffused radiation emergent from the phantom in (A). The attenuation values are plotted as the hills. In this plot the correspondence can be compared with the phantom object of (A).

that is not as accurately reconstructed is a "dark region" located between two sections of high-attenuation materials and towards the center of the object. This is to be expected for the two-dimensional object reconstruction because of radiation "blocking" in two dimensions. A more accurate reconstruction is obtained when using a three-dimensional reconstruction.

The image procedure generates additional images by mapping the computed  $f_{ij}$ ,  $b_{ij}$ , and  $s_{ij}$  coefficients. It is expected that the images



**Fig. 3.** (A) Characteristics of the attenuation of a cross section of a three-dimensional object (a phantom object). (B) Reconstructed attenuation in the presence of 5% multiplicative noise.

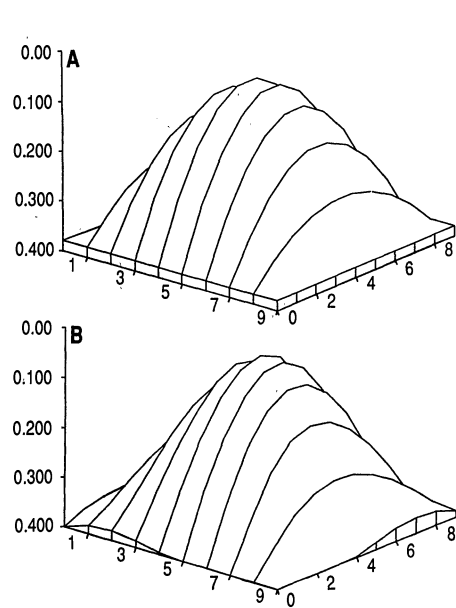


**Fig. 4.** (A) Characteristics of the forward-scattering coefficient of a cross section of a three-dimensional object (vertical axis pointing down). (B) Reconstructed forward-scattering coefficient of a section of a three-dimensional object in the presence of 5% noise.

based on the computed  $f_{ij}$ ,  $b_{ij}$ , and  $s_{ij}$  coefficients provides information not available from systems which measure only the attenuation of an object (corresponding to the  $w_{ij}$  coefficients), which is also computed by the present system.

Next we show a set of images generated with a simulation of a three-dimensional object modeled as a three-dimensional array of voxels. Figure 3A shows the attenuation characteristics of one slice (a two-dimensional section) of this object, and Figs. 4A and 5A show the forward and side-scattering characteristics of the object.

Using a set of modified measurement values, representing a 5% noise factor, we generated the attenuation and scattering coefficients for a phantom object 3A by means of the above-described inverse solution technique. Figures 3B, 4B, and 5B represent the attenuation, forward-scattering, and side-scattering characteristics of the reconstructed image of phantoms 3A, 4A, and 5A when the measurement values include a 5% noise factor. As can be seen, while the reconstructed images generated are affected by noise, the general characteristics of the object are still reconstructed quite well with a 5% noise factor. We have also done these reconstructions with no noise, 0.1% noise, and 1% noise. In these cases the reconstructions were much better, as one would expect. The no-noise case matched almost perfectly Figs. 3A, 4A, and 5A. We omit these pictures for lack of space.

We discuss now some mathematical issues

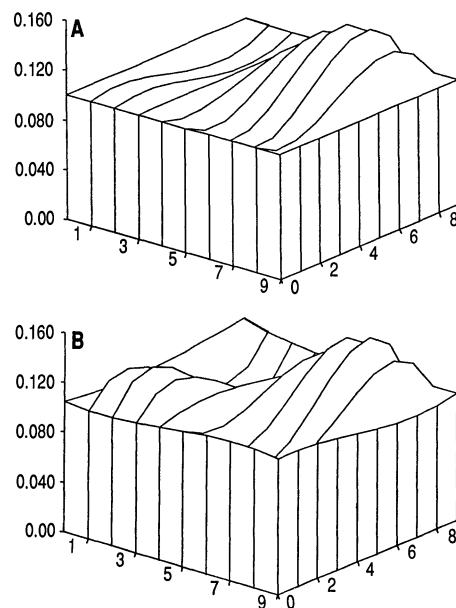


**Fig. 5.** (A) Characteristics of the side-scattering coefficient of a section of a three-dimensional object (a phantom object). (B) Reconstructed side-scattering coefficient of a section of a three-dimensional object in the presence of 5% multiplicative noise.

related to this problem. The method described in this article would not have been feasible without the computing power available in recent years. But even with powerful computers the large amount of computation requires effective algorithms. In the forward problem, the number of equations grows very quickly as the voxel size decreases. In fact, the number of equations is proportional to  $(L/\rho)^3$  where  $L$  is the length of the object and  $\rho$  is the voxel side. A few suggestions have been put forward in the direction of using iterative methods. The examples shown here made use of standard LU decomposition numerical routines in the solution of the forward problem. The forward problem is very well suited for parallel computations, since to do this one has to solve systems of the form  $Ax = \gamma$  for as many right-hand sides  $\gamma$  as detectors.

In the inverse problem, the method that we use is essentially a gradient descent technique. The classical problem here is to avoid being trapped in a local minima. One strong candidate is "simulated annealing." Simulated annealing has recently attracted the attention of the mathematical community due to its reported power to deal with a number of problems such as the traveling salesman problem and the optimal design of integrated circuits [see, for example, (7)].

The general methodology of our approach can be divided into three steps. First, we consider a discrete model describing the movement of particles in a fairly general medium. This model could be technically described as a two-step Markov process. It is not hard to see that it can also be looked upon as a discretization of an equation similar to the Boltzmann transport equation in the spatial and angular variables. Other models or partial differential equations describing propagation of radiation (such as the wave equation), could also be suitable for such an approach. Second, we develop algorithms for the solution of the forward problem. Third, we attack the reconstruction problem by minimizing the distance between the actual measurements and the computed solutions by varying the values of the coefficients of the linear system until an acceptable fit occurs. This methodology could certainly be applied to a number of models besides the one presented here.

This problem can also be easily cast as a neural network in which each voxel is represented by six neurons, one neuron for each direction of exit from the voxel. The activity of these cells corresponds to the radiation flux in a given direction and is equal to a weighted sum of the activity coming in from all six neighbors. Learning techniques such as back propagation (8) may have applications to these problems.

REFERENCES AND NOTES

1. A. M. Cormack, *Int. J. Appl. Phys.* **34**, 272 (1963); *Science* **209**, 1482 (1980).
2. G. Hounsfeld, *Br. J. Radiol.* **46**, 1016 (1973); *Science* **210**, 22 (1980).
3. D. C. Boyd *et al.*, *J. Comput. Asst. Tomog.* **6**, 202 (1982).
4. R. P. Feynman and A. R. Hibbs, *Quantum Mechanics and Path Integrals* (McGraw-Hill, New York, 1965), pp. 336–339.
5. See (4), pp. 20–24.
6. W. H. Press *et al.*, *Numerical Recipes, The Art of Scientific Computing* (Cambridge Univ. Press, New York, 1987), sections 10.5–10.10.
7. E. Aarts and J. Korst, *Simulated Annealing and Boltzmann Machines* (Wiley, New York, 1989).
8. D. E. Rumelhart and J. L. McClelland, *Parallel Distributed Processing* (Massachusetts Institute of Technology, Cambridge, MA, 1986), vol. 1.
9. We are grateful for the contributions of J. Coach, S. Davis, E. Elias, K. Johsens, G. Latham, J. Libove, J. Morse, H. Naparst, B. Parlett, V. Perez-Mendez, and C. Townes.

30 January 1990; accepted 3 April 1990

## Ultradeep (Greater Than 300 Kilometers), Ultramafic Upper Mantle Xenoliths

STEPHEN E. HAGGERTY AND VIOLAINE SAUTTER

Geophysical discontinuities in Earth's upper mantle and experimental data predict the structural transformation of pyroxene to garnet and the solid-state dissolution of pyroxene into garnet with increasing depth. These predictions are indirectly verified by omphacitic pyroxene exsolution in pyropic garnet-bearing xenoliths from a diamondiferous kimberlite. Conditions for silicon in octahedral sites in the original garnets are met at pressures greater than 130 kilobars, placing the origin of these xenoliths at depths of 300 to 400 kilometers. These ultradeep xenoliths support the theory that the 400-km seismic discontinuity is marked by a transition from peridotite to eclogite.

**D**IAMONDIFEROUS KIMBERLITES are widely recognized as hosts for a rich source of xenoliths from Earth's upper mantle (1). Study of these accidental inclusions have provided critical data on the composition, age, and evolution of parts of the upper mantle as well as on the origin of diamonds (2). The deepest samples from the upper mantle are considered to be sheared garnet lherzolites (composed mostly of olivine, orthopyroxene, and clinopyroxene) that were sampled by kimberlites from the stable mantle lithosphere at depths no greater than 180 km (3). Whether the mobile and deeper asthenosphere is ever sampled in kimberlite eruptives remains uncertain (4). A precise knowledge of the mineralogy and petrology of the deeper (>200 km) upper mantle is needed to account more rationally for the nature of seismic discontinuities and other geophysical properties and for verification of the results of high-pressure experiments (5).

Direct access to ultradeep samples is also required in the face of the growing debate on the nature of subduction in the Archean and on whether downgoing oceanic crustal slabs become buoyant at the 650 km discontinuity (6, 7) or continue to the core-mantle boundary (8). Subducted oceanic crust,

which is largely basaltic in composition, is predicted to transform to eclogite (Na-rich clinopyroxene and Fe-Ca-Mg-rich garnet) with increasing depth, but eclogites in kimberlites may also form by low-pressure partial melting of garnet lherzolite (9). The

origin of eclogites is by no means settled (10), nor are the propositions that the deeper asthenosphere is composed of piclogite [olivine-bearing eclogite (11)] or alternatively of garnetite [garnet and the solid-state transformation of pyroxene to the garnet structure, (12)], both of which require high temperatures and depths exceeding 300 km.

Conversion of low-pressure pyroxene to the garnet structure, or the solid-state dissolution of pyroxene in garnet, requires that some of the Si in fourfold tetrahedral ( $\text{Si}^{\text{IV}}$ ) coordination at low pressure be converted to sixfold octahedral ( $\text{Si}^{\text{VI}}$ ) coordination, which is indicative of high pressure (13). Because the ratio of Si to O in pyroxene is 4:12 rather than the garnet value of 3:12, the chemical signature of this high pressure substitution is more than 3 Si atoms per 12 O atoms (14, 15). Although solid solution of pyroxene in garnet was demonstrated experimentally more than 20 years ago (16), naturally occurring analogs have only recently been recognized in diamond inclusions from South Africa (17) and Brazil (18).

We have now identified xenoliths similar to the mineral inclusions from diamond that have eclogitic affinities and large concentrations of omphacite (diopside-jadeite solid solution) exsolved in pyropic garnet. The xenoliths were collected from coarse (1 to 5 cm) heavy media concentrates resulting from commercial diamond recovery at the Jagersfontein kimberlite, 230 km southeast of Kimberley, South Africa (19). Two xeno-

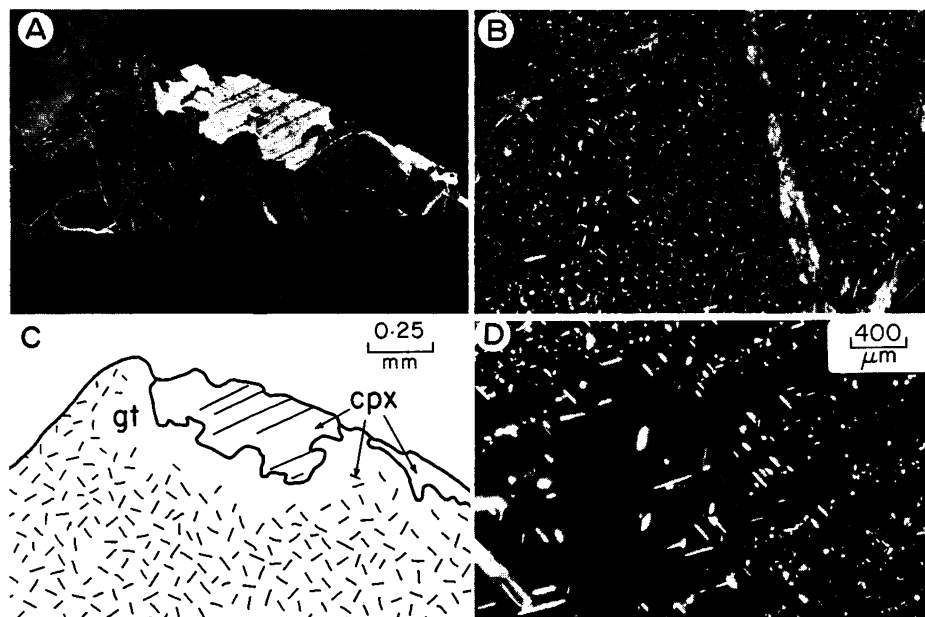


**Fig. 1.** Photomicrographs of garnet (gt) with exsolved clinopyroxene (cpx) along crystallographically controlled planes. (A), (C), and (D) are from sample JX-25 and (B) is from JX-50. The sketch in (C) schematically illustrates the ordered distribution of clinopyroxene lamellae in the garnet and the increase in the number of lamellae with distance from the larger clinopyroxene grain; note the irregular geometry of the grain boundary contact between garnet and clinopyroxene and the lamellae-free diffusion zone. Bright veinlets are cracks filled by secondary calcite, mica, and amphibole. The millimeter scale applies to (A), (B), and (C), and the micrometer scale to (D).

S. E. Haggerty, Department of Geology, University of Massachusetts, Amherst, MA 01003.  
V. Sautter, Laboratoire de Géophysique et de Géodynamique Interne, Université de Paris-Sud, 91405 Orsay Cedex, France.